



# Effects of process parameters on porosity in laser powder bed fusion revealed by X-ray tomography

Anton du Plessis<sup>a,b,\*</sup>

<sup>a</sup> Physics Department, Stellenbosch University, Stellenbosch, 7602, South Africa

<sup>b</sup> CT Scanner Facility, Stellenbosch University, Stellenbosch, 7602, South Africa



## ARTICLE INFO

### Keywords:

Additive manufacturing  
Laser powder bed fusion  
X-ray tomography

## ABSTRACT

This paper reports on X-ray tomography of a series of coupon samples (5 mm cubes) produced under different process parameters, for laser powder bed fusion of Ti6Al4V. Different process parameters result in different pore formation mechanisms, each with characteristic pore sizes, shapes and locations within the 5 mm cube samples. While keyhole pores, lack of fusion pores and metallurgical pores have been previously identified and illustrated using X-ray tomography, this work extends beyond prior work to show how each of these not only exist in extreme situations but how they vary in size and shape in the transition regimes. It is shown how keyhole mode porosity increases gradually with increasing power, and how this depends on the scan speed. Similarly, lack of fusion pores are shown to occur following scan tracks in situations of poor hatch overlap, or a similar but different distribution of lack of fusion porosity due to large layer height spacing, showing respectively vertical and horizontal lack of fusion pore morphologies. Increased spacing between hatch scan tracks and contour scan tracks is demonstrated to form a near-surface porosity similar to that previously reported for slowing at the end of scan tracks which can cause keyhole mode porosity. Insights from 3D images allow improvements in parameter choices for optimized density of parts produced by laser powder bed fusion, and generally allow a better understanding of the porosity present in additively manufactured parts.

## 1. Introduction

Additive manufacturing (AM) of metals and particularly laser powder bed fusion (LPBF) has seen significant growth in recent years, with associated improvements in material quality, density and subsequently also improved mechanical properties – a recent comprehensive review of the technology is presented in [1]. Driven by applications in industries such as medical and aerospace, which require extremely high quality and reliable parts, there have been significant efforts at optimizing processes and ensuring superior mechanical properties, with great success [2–6]. Especially the biomedical titanium alloy Ti6Al4V has been studied widely with reported excellent mechanical properties when processes have been optimized, see for example [7].

With the development of AM and its wider adoption, there is an ever-increasing design complexity that is sought after for functional end-use parts [8]. Therefore, quality control requirements increase in importance and becomes challenging due to the complexity. There is a long list of possible errors, flaws and imperfections in the LPBF manufacturing process, which can all lead to compromised mechanical properties [1]. This has led to variability in the resulting mechanical

properties reported, especially in earlier studies. There has been found especially large scatter in fatigue tests, and also differences in yield strength and elongation to failure in static tensile tests [9]. These may be attributed to three main causes: unwanted residual stress, poor microstructure, or the presence of porosity or inclusions in the material [10]. As quality control in AM improves and an improved understanding of the LPBF process develops, the role of porosity is increasingly recognized. The effects of excessive porosity has been shown to reduce mechanical properties, for example in a recent study of LPBF of Ti6Al4V as-built samples, it was shown how the tensile strength and elongation to failure varies with process parameters which create different forms of pores [11]. The role of pores, inclusions and surface defects on fatigue life of metals has been reviewed recently [12–14] where it is shown that pores, especially those near the surface are critical and act as crack initiators. Quality control of porosity in parts by using X-ray tomography and/or metallurgical cross-sections is already widely adopted [15–18]. Additionally, quality control at all levels of the process is critical, from powder feedstock, to process parameters, shielding gas, stress-relief heat treatment and other post-process treatments.

\* Corresponding author at: Physics Department, Stellenbosch University, Stellenbosch, 7602, South Africa.

E-mail address: [anton2@sun.ac.za](mailto:anton2@sun.ac.za).

<https://doi.org/10.1016/j.addma.2019.100871>

Received 3 June 2019; Received in revised form 16 July 2019; Accepted 10 September 2019

Available online 19 September 2019

2214-8604/ © 2019 Elsevier B.V. All rights reserved.

In general, the optimal process parameters for LPBF of a specific material are best found by considering single track formation at a range of laser power densities and finding the best regime for stable single track formation – the basic building block of the process. This has been done with great success as described in [19–22]. This is especially useful when developing new materials and makes it simple to separate different regimes to find the best and most stable parameters for the LPBF process – a single track with sufficient penetration (depth) into the underlying layer for good fusion, a good width for efficient processing (too narrow will require smaller hatch spacing requiring much longer build times) and stable, even and continuous track formation. When multiple tracks and layers are created to build 3D objects, the process remains stable resulting in a good part. The hatch spacing between adjacent tracks and the build height of successive layers must be optimized considering the size, depth and shape of the single track.

Despite this optimization, various types of pores may be created in the LPBF process. Different pore formation mechanisms have been identified in LPBF, with the three most common forms related to process parameters being keyhole mode pores, metallurgical or gas pores and lack-of-fusion pores [23]. Keyhole mode porosity occurs when the energy density is too high (e.g. high power or slow speed), creating a vapour depression in the deep melt pool with high liquid flow velocity, which closes in on itself and traps vapours as the melt pool propagates forward [24]. This results in large rounded but not perfectly spherical pores. Lack of fusion pores occur when the energy density is too low (low power or high speed), causing insufficient fusion of material and which results in irregular pores with varying sizes and with sharper edges and flattened shape, and sometimes containing entrapped unmelted particles [25]. In the intermediate regime of energy density (conduction mode), gas porosity of very small sizes with spherical shape occurs and this has been attributed to gas entrapment of shielding gas, porosity of powder particles, or alloy vapours inside the molten pool [1].

In addition, high scanning speeds coupled with insufficient laser power leads to balling effects in individual tracks due to melt pool viscosity and surface tension effects causing the track to break into beads, which can lead to uneven powder spreading and insufficient melting in the next layer. On the other hand, low scanning speeds coupled with low power can lead to break-up of melt tracks due to the smaller melt pool near its threshold for melting thus not forming a continuous track [26]. In addition to these effects, denudation zones where powder is removed from the front or sides of the melt pool due to melt pool dynamics or gas flow, can create uneven melting and irregular tracks, and particle spatter may also cause irregularity – for example the spatter falling on an unmelted area of the powder bed will shield the underlying powder from the laser [27,28]. These and other causes of porosity and flaws in LPBF are described in more detail in [29]. There have also been numerous efforts at modelling the melt pool dynamics which reveal information on pore formation, and on macroscale simulation for prediction of porosity formation [27,30–32].

There have been high-resolution X-ray tomography imaging studies covering a range of process parameters showing lack of fusion and keyhole mode pores using synchrotron radiation [37,38]. The use of laboratory X-ray tomography for detailed analysis of AM materials was reviewed recently and also summarizes various efforts at imaging different porosity types [39]. The analysis of porosity due to electron beam melting with different scan strategies was reported in [40] and similarly for LPBF [41].

Porosity formation has been studied in real time with great success using fast X-ray imaging with synchrotron sources. This includes studies of the melt pool dynamics showing keyhole pore formation and particle spatter [33], defect and melt pool dynamics showing pore formation mechanisms and effects of denudation zones [34], and threshold for keyhole vapour depression formation [35], the formation of keyhole mode pores at the end of scan tracks due to slowing of the laser and increased power density [36], amongst others. What is important to

note is the recent discovery that the threshold for vapour depression formation is lower than expected and the fact that vapour depressions are therefore present across the entire range of typical LPBF process parameters [35], but that the formation of pores occurs only when the vapour depression becomes deep and unstable.

Many commercial systems already have an optimized process parameter set for typical AM materials such as Ti6Al4V, allowing near fully dense parts with minimal porosity. This results, in combination with suitable microstructure, in excellent mechanical properties as demonstrated for example in [7]. However, an understanding of the porosity formation in 3D parts is useful to further improve the processes and find new ways of reducing the formation of these pores. Understanding the formation of porosity, pore shapes and distributions can assist in quality control efforts, to know what is wrong in the system, for appropriate corrective action (e.g. laser power drop causing lack of fusion pores). Since adjacent tracks and subsequent layers overlap, remelting occurs and this may contribute to minimizing porosity, or modifying the shape of the final resulting porosity distributions. An understanding of the resulting pore sizes and distributions is valuable for “forensic” analysis of porosity distributions found in built parts.

In this paper we report on a detailed X-ray tomography study of 5 mm cubes of Ti6Al4V produced under different process parameters of a commercial system. The aim of this study is to provide detail and insight into the typical porosity formation regimes and the resulting pore formation sizes, extents and shapes of pores over a large range of porosity values, for a typical LPBF system and for final built parts. Variation of laser power at different scan speeds show the regimes of lack-of-fusion, conduction mode and keyhole mode porosity with porosity levels all the way from below 0.01% up to more than 10%. The low-power threshold for lack of fusion porosity is very sharp and varies as expected for different scan speeds. Contrary to previous reports, the onset and increase in detectable keyhole mode porosity at increasing power is gradual, and not as sharp as the transition to lack-of-fusion. Comparing scan speeds, there is a stronger increase (higher slope) in keyhole mode porosity formation for slower scan speed. This is in agreement with results of [35] where it was shown that keyhole vapour depressions are suppressed at higher velocity. This shows that a larger window of “low porosity” is present in the case of faster scan speed, but the threshold for lack of fusion is higher, requiring a higher power laser (or smaller spot size).

A secondary goal of this work was to produce a series of high quality 3D images of different pore types found in final produced parts, as the previously reported morphologies vary significantly, and a holistic collection of images from a range of process parameters for the same material on the same system is deemed valuable to an improved understanding and further development of the technology. This should be useful for positive identification of pore types in quality control efforts using microCT and might assist in the efforts advancing towards (almost) fully dense and reliable production of parts.

## 2. Materials and methods

Laser powder bed fusion of Ti6Al4V ELI was performed with the EOS M290 system installed at Executive Engineering Pty (Ltd), based in Cape Town, South Africa. The system uses EOS-supplied Ti6Al4V ELI powder with D90 size value measured using laser diffraction according to ISO 13320-1 as 50.0  $\mu\text{m}$ . Optimal process parameters for this system which was used as the benchmark setting is 280 W laser power, 1200 mm/s scan speed, 0.14 mm hatch spacing, 0.03 mm layer height, contouring is employed in two tracks around all edges, spaced by 0.015 mm from the hatch pattern. A stripe scanning strategy was used where 5 mm wide sections are scanned at a time. The powder bed temperature was held at 35 °C and the stripe overlap was by default zero – this means the next stripe starts with a scan track exactly overlapping the previous track from the previous stripe. A total of 30 cubes were printed in three batches, in flat orientation (no rotation or support

**Table 1**  
Description of experiments conducted – different parameter sets.

	Power (W)	Scan speed (mm/s)	Hatch-contour spacing (mm)	Layer height (mm)	Hatch spacing (mm)
Variation of power at nominal scan speed, across a wide range	From 100 to 364 (9 values)	1200	0.015	0.03	0.14
Variation of power at slower scan speed, across a wide range	From 90 to 360 (8 values)	800	0.015	0.03	0.14
Variation of spacing between hatch and contour tracks	280	1200	0.015; 0.0225; 0.03; 0.05; 0.1; 0.15	0.03	0.14
Variation of layer height	280	1200	0.015	0.03; 0.06	0.14
Variation of hatch spacing	280	1200	0.015	0.03	0.14; 0.17; 0.2; 0.23

structures) with various selected parameters as summarized in [Table 1](#) below. Each 5 mm cube was wire-cut from the baseplate, without any stress relief heat treatment.

The cubes were microCT scanned at the Stellenbosch University CT Facility [43] using a modified version of the standard protocol described in [44]. The X-ray voltage and current was 200 kV and 50  $\mu$ A respectively, with a voxel size of 10  $\mu$ m and no beam filters used due to the small penetration depth, and the sample was scanned at 45 degrees in both axes relative to the beam direction, to minimize cone beam artefacts on the flat edges of the cube. Beam hardening correction factor of 9 was applied in the Datos reconstruction software, to minimize beam hardening on the edges and obtain nearly even greyscale across the entire cube. Images were analyzed in Volume Graphics VGSTUDIO MAX 3.2. This process involves an initial surface determination (including “remove all particles and voids” option) to determine the exterior edge of the sample, followed by image registration (turning images upright in slice views). This was followed by selecting the cube as a region of interest (ROI) and applying an erosion function of 3 voxels (removing 3 voxels from the edge all around) and creating a new volume based only on the cube without any exterior air and the thin layer of edge voxels. This new volume has its own greyscale histogram easing the segmentation process for the pores. The segmentation process uses a manual thresholding based on placing the threshold value to the left of the main material histogram peak – the intersection between pore space (air) and material peak is visible and segmentation can be checked visually across all slices to confirm the validity of the choice. In addition, a local gradient optimization (surface determination advanced mode) is employed to minimize the effect of manual bias or variations in greyscale intensity across the image. This process allows accurate porosity values to be determined for all pores in each cube with a total voxel count of more than 8 ( $2 \times 2 \times 2$ ). For a spherical pore space, the diameter of the smallest detected pore is therefore 20  $\mu$ m. [Table 1](#) below provides a summary of the experimental parameter variations while supplementary material provides more details of every sample.

### 3. Results and discussion

When the laser power is varied at a constant scan speed, with all other parameters at their default values, it can be expected that at lower power, the melt pool and hence scan track is thinner and shallower, causing lack of fusion between adjacent tracks and between subsequent layers. This is clearly seen in the first image in [Fig. 1](#) which shows slice images viewed from the top of the cube. As the power increases (in this series of images for 800 mm/s), there is an optimal value in terms of porosity reduction, followed by a gradual increase in randomly dispersed pores with roundish shapes. These roundish pores are attributed to keyhole mode porosity, when too high laser power causes a deep melt pool with strong melt pool dynamics causing entrapment of vapours in pores as the melt pool propagates forward and the vapour cavity collapses. In the intermediate regime where porosity is minimized, small spherical pores are found only – these are presumably metallurgical pores which are due to trapped gas from between powders. In the series of images in [Fig. 1](#) it is clear that the keyhole mode porosity increases in extent with increasing power at 800 mm/s. The quantitative porosity values are plotted in [Fig. 2](#), showing power variation for two scan speeds 1200 mm/s and 800 mm/s. This shows, as expected, that the optimal power for minimal porosity is lower at lower scan speed. It can be understood that a slower moving beam requires less power to create the same size melt pool. What is interesting to note here is that for both scan speeds, there are clear thresholds below which lack of fusion become predominant, but no clear threshold for keyhole mode porosity formation. This is consistent with recent high speed imaging work where it was demonstrated that vapour depressions are present in the melt pool for all process parameters above a threshold value, but that keyhole pores are only present when the vapour depression

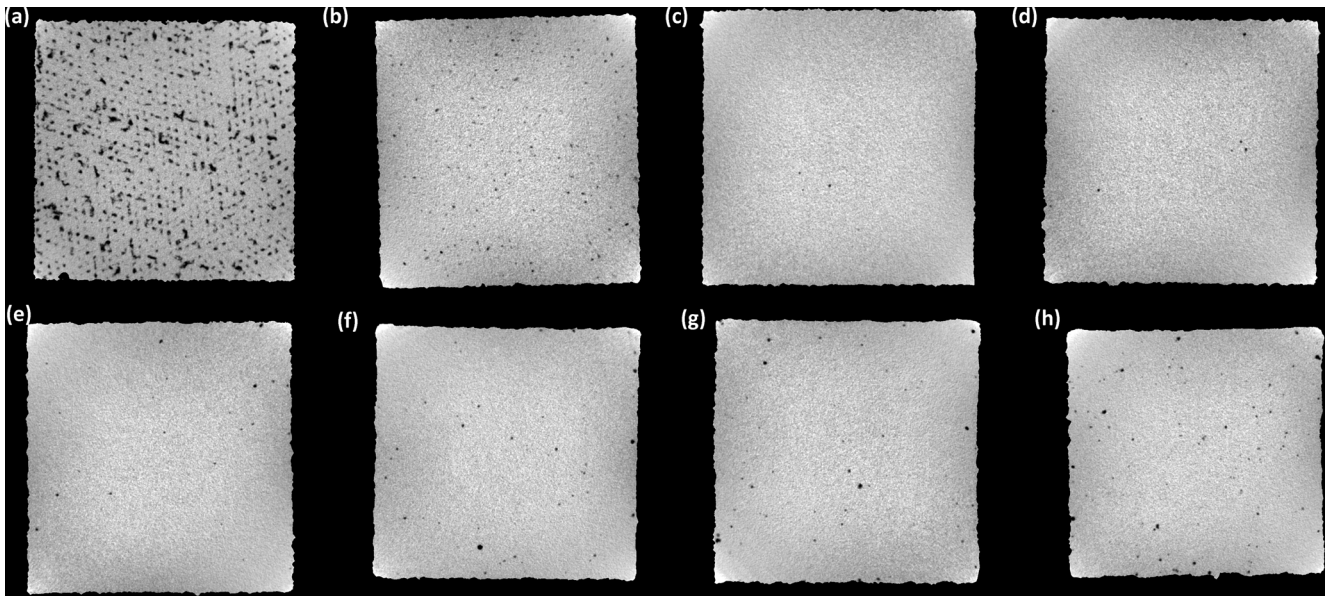


Fig. 1. Series of 5 mm cubes for increasing power shown in CT slice images. This is the second experiment in Table 1 (800 mm/s and power from 90 to 360 W).

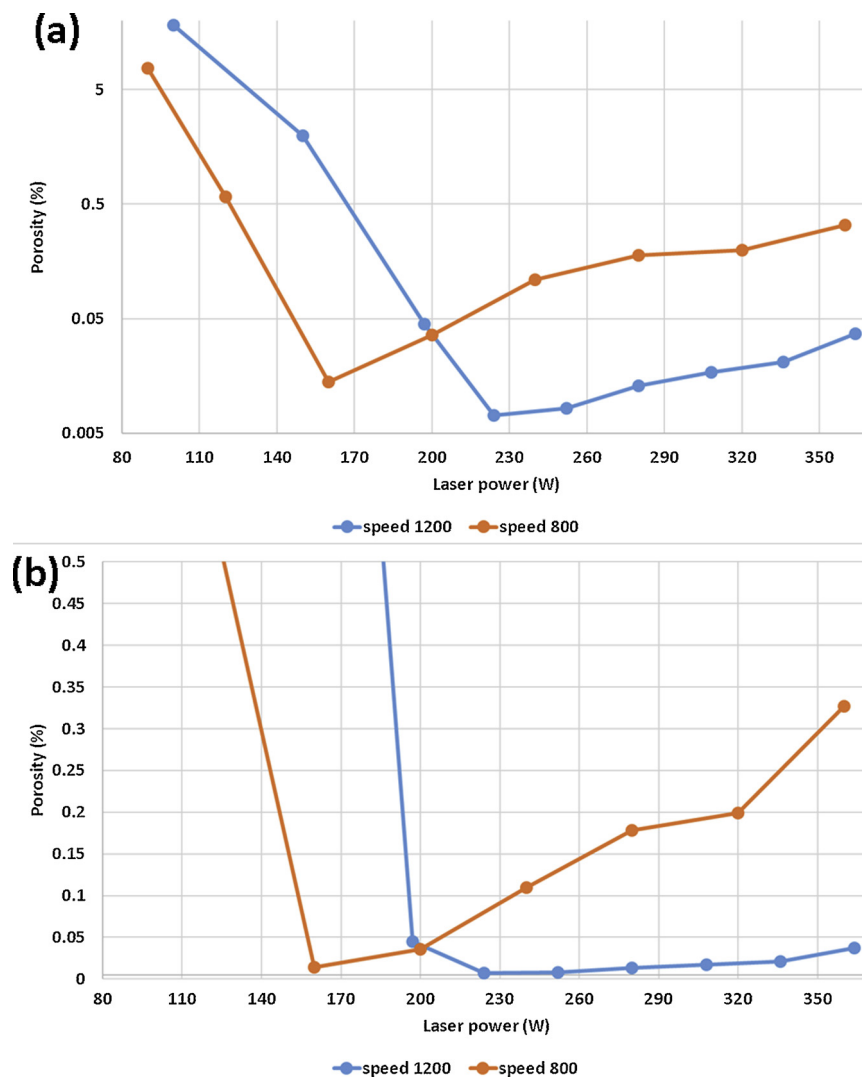
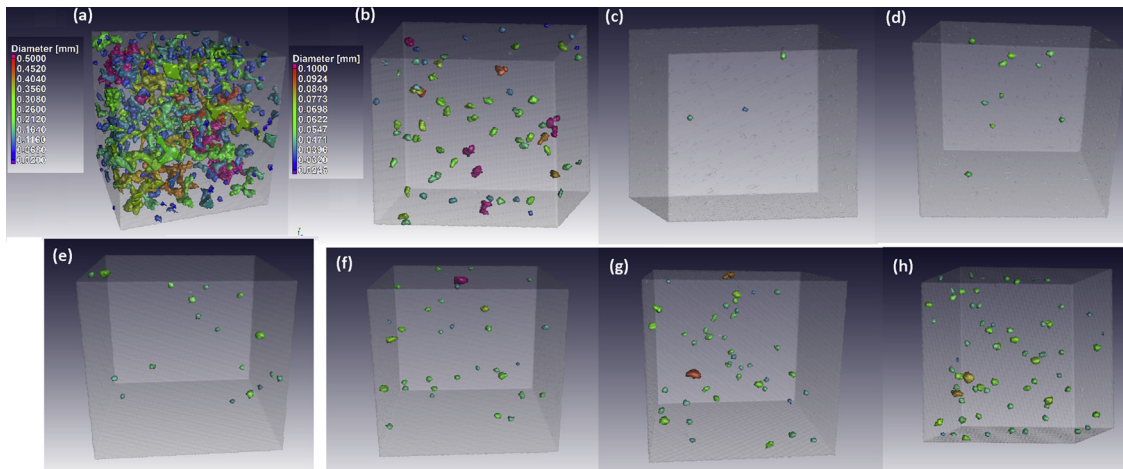


Fig. 2. Porosity values as a function of power for two scan speeds, from microCT scan data. Note the log scale in (a). In (b) is shown the same data on a linear scale focusing on the lower porosity values.



**Fig. 3.** 3D porosity distributions in the central 1 mm of each of the samples in Fig. 1, at increasing power from 160 W to 360 W (800 mm/s). Shown here are  $1 \times 1 \times 1$  mm selected cube regions in 3D. The images (b)–(h) are all to the same colour scale maximally 0.1 mm.

becomes unstable at higher power [35]. What these results show additionally is that the resulting keyhole mode pores increase in extent and in size with increasing power – this is understandable as the higher power likely results in a larger vapour cavity.

It is further interesting that the keyhole mode porosity formation increase with power (the slope) varies with scan speed. It seems higher power and speed allows a wider “safe” process parameter range with less extensive keyhole mode porosity – the higher speed suppresses instability in the vapour depression, also consistent with reports in [35].

The increase in keyhole mode porosity seen in Figs. 1 and 2 was further analyzed for the region from 90 W to 360 W for 800 mm/s. Images of a selected 1 mm cube section in the middle of each of these samples is shown in Fig. 3. Fig. 3(a) and (b) show lack of fusion pores, porosity is minimized in (c) and keyhole mode pores increase in size and extent in (d) to (h), with increasing power. There seems to be a trend of increasing pore size, but this could be affected by remelting (which should make pores smaller they should have been).

In Fig. 4 is shown close-up views of the largest individual pores in the three major regimes – lack of fusion, conduction mode and keyhole mode, all on the same scale. This shows clearly the irregular shape of lack of fusion porosity (a), which is in this case vertical (in the build direction) due to inter-track lack of fusion. The metallurgical pore (b) is near-spherical and the keyhole mode pore (c) is rounded but not spherical.

Variation of the hatch spacing between adjacent tracks was performed at 280 W and 1200 mm/s – it is expected that as the spacing

increases, less overlap and less remelting occurs eventually resulting in lack of fusion between adjacent tracks. This is clearly visualized in Fig. 5 with quantitative porosity analysis values, and 2D and 3D images of the extreme case of 0.6% porosity at 0.23 mm spacing (nominal value is 0.14 mm).

The variation of layer height from 0.03 (nominal) to 0.06 mm shows a similar effect as above whereby the subsequent layers do not fuse properly causing horizontal lack of fusion porosity as visualized in Fig. 6. Fig. 6 shows the increased porosity (a), a slice image (b), a 3D image of the cube (c) and a close-up of the largest horizontal lack-of-fusion pore (d).

Porosity around the edges of parts (subsurface) have been observed often, see for example recent work in a round robin test where this was observed [18]. The formation of subsurface pores near the contours may in some cases be due to the laser spot slowing before turning around – this causes an increase in power density resulting in keyhole mode formation at the end of scan tracks – this was visualized in a recent experiment using fast X-ray imaging [36]. This form of porosity was not observed in the present experiments, but the spacing between hatch scan tracks and the contour tracks could be varied. This variation causes a similar near-surface porosity distribution as shown in Fig. 7 for 0.05 mm hatch offset value (nominal is 0.015 mm). Fig. 8 shows slice images from this and wider spacing in simple slice images and also in accumulative images exaggerating the porosity which shows the distribution clearly around the edges.

Further investigation of extensive lack of fusion at low power clearly shows the pores are regularly spaced (by a distance roughly equal to the

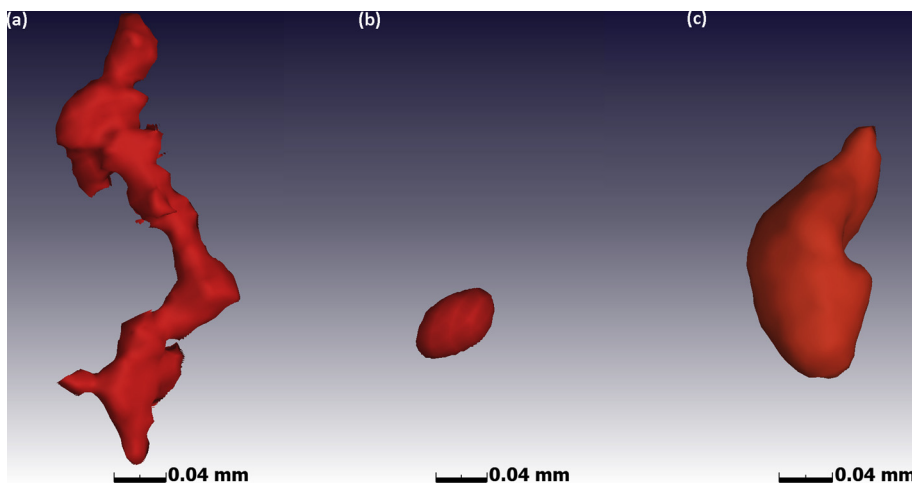


**Fig. 4.** Pore morphologies in different regimes are shown here on the same scale for (a) lack of fusion, (b) conduction mode (metallurgical pore) and (c) keyhole mode pores taken from the largest pores in the samples at 800 mm/s, power values 120 W, 160 W, 360 W. All images are vertical (build direction is upwards) – this indicates the lack of fusion is in this case between adjacent tracks primarily – sometimes this is between subsequent layers, making it horizontal but similarly irregular with sharp edges. Build direction is vertical in all images.

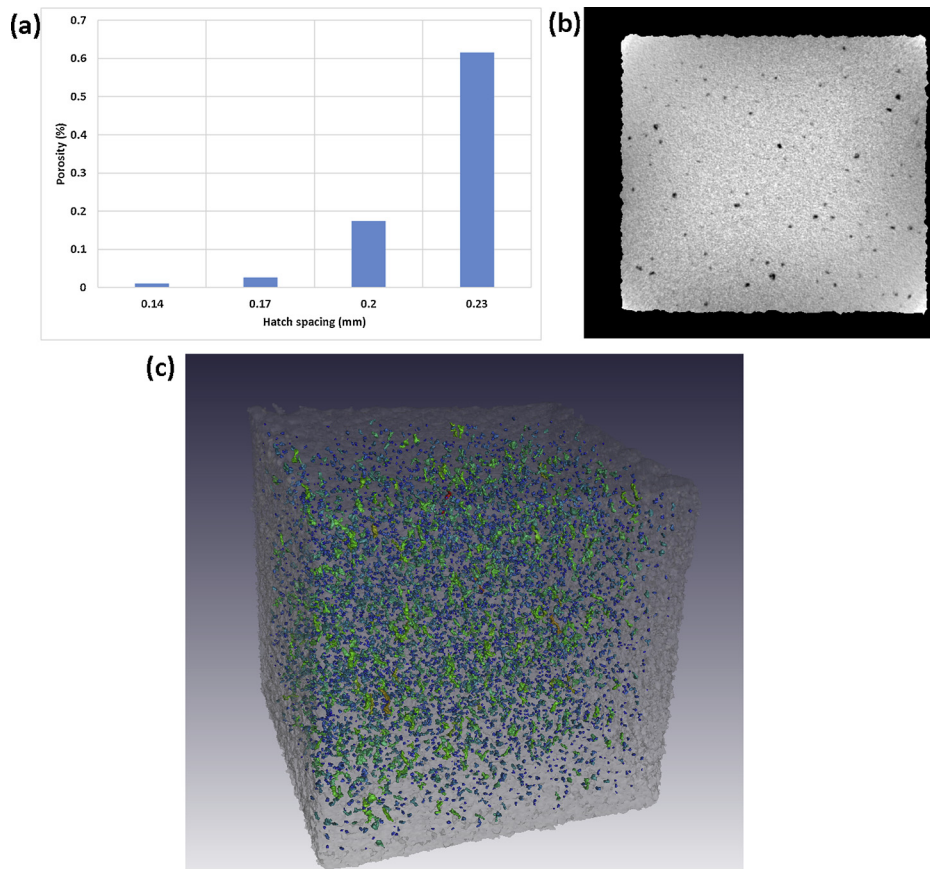


Fig. 5. Effect of hatch spacing increase – wider spacing between adjacent tracks results in higher porosity values – a form of lack of fusion occurs between tracks (vertical oriented pores).

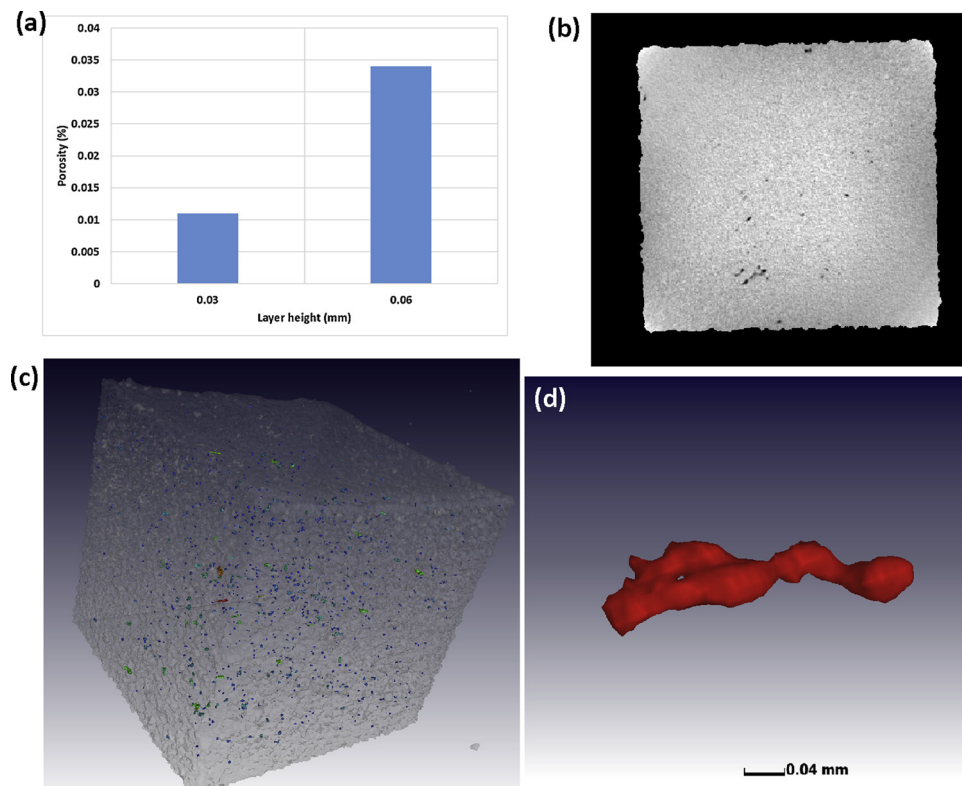


Fig. 6. Effect of increased layer height – causing lack of fusion pores with horizontal morphology.

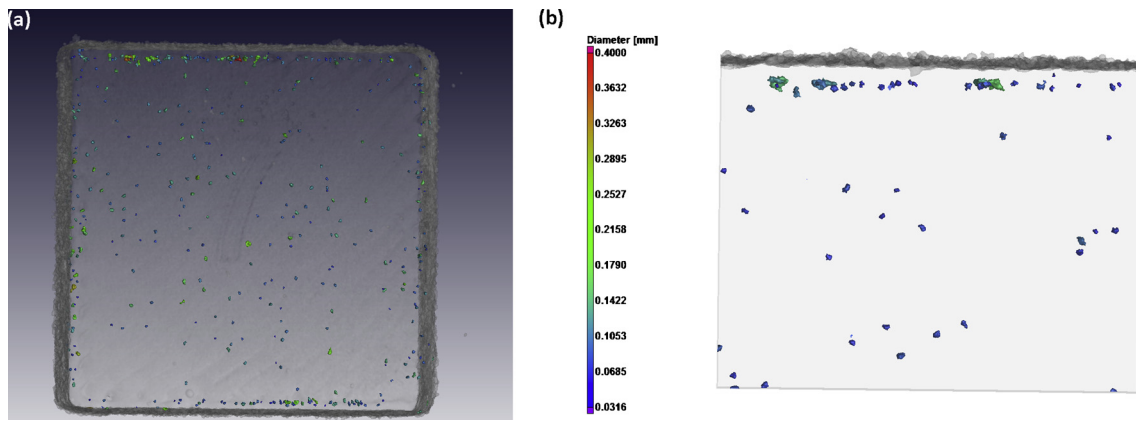


Fig. 7. Porosity at contours (but sub-surface) due to wide hatch-contour spacing (0.05 mm in this case). No such contour porosity was observed at 0.015 mm. (a) shows entire cube and (b) shows a close-up view.

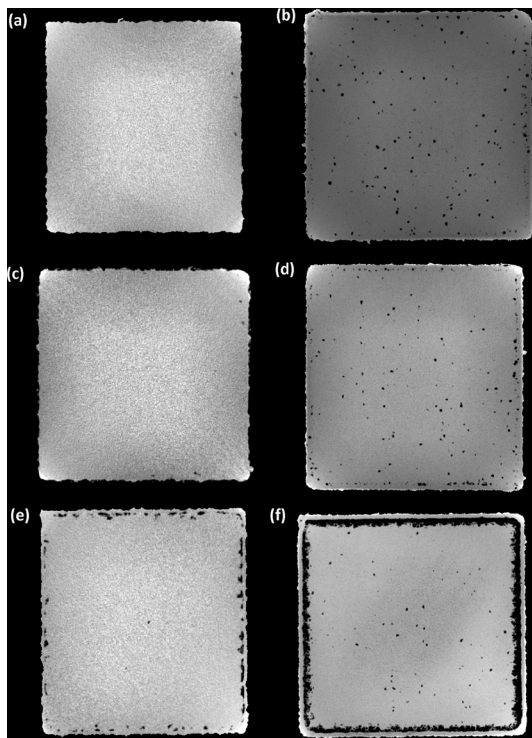


Fig. 8. Variation between hatch and contour tracks in increasing order from top to bottom 0.03; 0.05; 0.10 mm. Each parameter set is shown in two ways: (left) a representative slice image – the usual CT cross sectional view, and (right) a thick-slab image showing all pores in a 3 mm thick section viewed from the top (all slices are added to one image with pores overlapping in the same region making larger dark areas).

track width) and the angle between subsequent layers (67°) is also detected in the pore distribution as shown in Fig. 9. In one layer the lack of fusion pores follow the scan tracks (probably continuously), but as the next layer is formed at a different angle, remelting occurs in the overlap areas of the current and previous layer, closing some of the pores along the previous track. This results in structured pores spaced by a distance equal to the scan track width, and at an angle equal to the layer angle change in discontinuous lines.

In the work reported here, no other trends could be observed related to increased porosity in specific areas. As mentioned in the methods section, the scan strategy uses stripes of 5 mm width, with zero offset between stripes. A potential source of porosity could be at the boundary between stripes, especially if the previous stripe area has been allowed

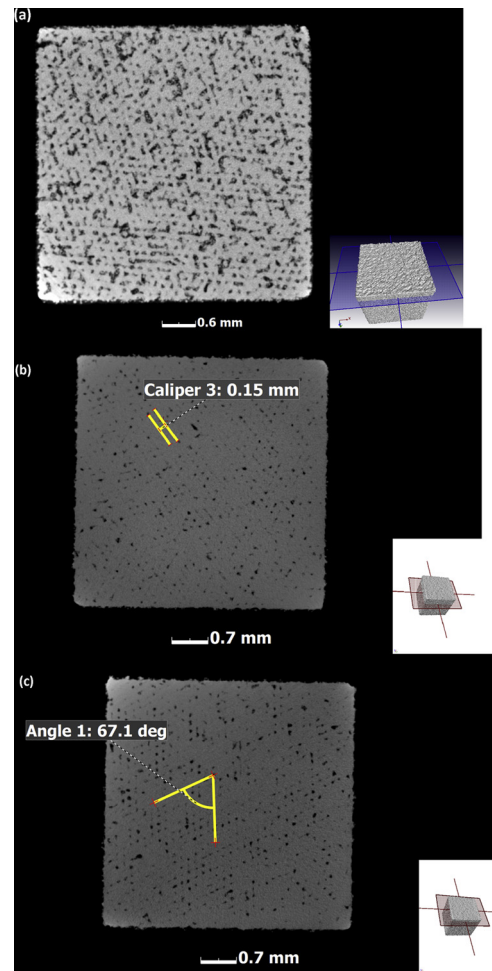


Fig. 9. Porosity patterns due to lack of fusion (low power), seen in slice images where (a) is 100 W and contains unmelted powder particles in void spaces (b) at 150 W with structured porosity spacing shown ~0.15 mm, (c) combined pores of two layers showing 67° rotation between layers. These porosity patterns occur due to the melt pool becoming too small and hence lack of fusion between scan tracks.

to cool down. However, no such effects were observed in the results, potentially due to the layer-by-layer rotation strategy, also by the remelting of previous regions at the stripe boundary. As shown in the supplementary material, three builds were done with different cube locations on build plate, and parameters as described. All data is

provided and mesh representations of porosity of every cube is supplied.

#### 4. Conclusions

A comprehensive experimental campaign was conducted to visualize pore formation regimes in a typical commercial metal AM system using X-ray tomography. The results assist in understanding the typical porosity extent, pore shapes and distributions in a commercial LPBF system. The lowest porosity regime is shown to be in a narrow range, with the threshold for lack of fusion being very sharp and the formation of keyhole mode pores showing only a gradual increase with power. The keyhole pores increase in number and size with increasing power, but at higher scan speed the keyhole pore formation is suppressed and its onset is therefore only at higher power. The safe processing window is therefore larger at higher scan speed. Besides this, various other distributions of porosity have been visualized and described. Contour porosity was shown to occur due to larger spacing between hatch and contour tracks, with a similar distribution as that reported previously for a slowing beam at the end of scan tracks. Structured pores were demonstrated with a spacing at the track width and in lines at angles corresponding to the inter-layer angular rotation of the system. These results assist in providing more insight into pore formation mechanisms and may assist in correct diagnosis of porosity types in non-destructive test and quality control efforts. Future work might include similar investigations of complex geometries, varied build angles, downsink surfaces and the potential for porosity variations with height corresponding to temperature build-up. Such work has the potential to yield practical solutions to mitigate porosity formation, by process parameter variations varied due to geometry of part.

#### Acknowledgements

The South African Department of Science and Technology is acknowledged for support through the Collaborative Program for Additive Manufacturing (CPAM). I would like to acknowledge fruitful and useful discussions with Dr Ina Yadroitsava, and for reading the manuscript. Executive Engineering (Pty) Ltd is acknowledged for producing the samples used in this study, special thanks go to Pierre Conradie and Coenraad Eygelaar for their support in this process.

#### Appendix A. Supplementary data

Supplementary material related to this article can be found, in the online version, at doi:<https://doi.org/10.1016/j.addma.2019.100871>.

#### References

- [1] T. Debroy, H.L. Wei, J.S. Zuback, T. Mukherjee, J.W. Elmer, J.O. Milewski, A.M. Beese, A. Wilson-Heid, A. De, W. Zhang, Additive manufacturing of metallic components – process, structure and properties, *Prog. Mater. Sci.* 92 (2018) 112–224, <https://doi.org/10.1016/j.pmatsci.2017.10.001>.
- [2] D.D. Gu, W. Meiners, K. Wissenbach, R. Poprawe, Laser additive manufacturing of metallic components: materials, processes and mechanisms, *Int. Mater. Rev.* 57 (2012) 133–164, <https://doi.org/10.1179/1743280411Y.0000000014>.
- [3] M. Qian, W. Xu, M. Brandt, H.P. Tang, Additive manufacturing and postprocessing of Ti-6Al-4V for superior mechanical properties, *MRS Bull.* 41 (2016) 775–784, <https://doi.org/10.1557/mrs.2016.215>.
- [4] D. Herzog, V. Seyda, E. Wycisk, C. Emmelmann, Additive manufacturing of metals, *Acta Mater.* 117 (2016) 371–392, <https://doi.org/10.1016/j.actamat.2016.07.019>.
- [5] D. Bourell, J.P. Kruth, M. Leu, G. Levy, D. Rosen, A.M. Beese, A. Clare, Materials for additive manufacturing, *CIRP Ann. Manuf. Technol.* 66 (2017) 659–681, <https://doi.org/10.1016/J.CIRP.2017.05.009>.
- [6] M. Schmidt, M. Merklein, D. Bourell, D. Dimitrov, T. Hausotte, K. Wegener, L. Overmeyer, F. Vollertsen, G.N. Levy, Laser based additive manufacturing in industry and academia, *CIRP Ann. Manuf. Technol.* 66 (2017) 561–583, <https://doi.org/10.1016/J.CIRP.2017.05.011>.
- [7] I. Yadroitsev, P. Krakhmalev, I. Yadroitsava, A. Du Plessis, Qualification of Ti6Al4V ELI alloy produced by laser powder bed fusion for biomedical applications, *JOM* 70 (2018) 372–377, <https://doi.org/10.1007/s11837-017-2655-5>.
- [8] A. du Plessis, C. Broeckhoven, I. Yadroitsava, I. Yadroitsev, C.H. Hands, R. Kunju, D. Bhate, Beautiful and functional: a review of biomimetic design in additive manufacturing, *Addit. Manuf.* (2019), <https://doi.org/10.1016/J.ADDMA.2019.03.033>.
- [9] J.J. Lewandowski, M. Seifi, Metal additive manufacturing: a review of mechanical properties, *Annu. Rev. Mater. Res.* 46 (2016) 151–186, <https://doi.org/10.1146/annurev-matsci-070115-032024>.
- [10] U. Zerbst, K. Hilgenberg, Damage development and damage tolerance of structures manufactured by selective laser melting – a review, *Procedia Struct. Integr.* 7 (2017) 141–148, <https://doi.org/10.1016/j.prostr.2017.11.071>.
- [11] S. Zhang, S. Rauniyar, S. Shrestha, A. Ward, K. Chou, An experimental study of tensile property variability in selective laser melting, *J. Manuf. Process.* (2019) 1–10, <https://doi.org/10.1016/j.jmapro.2019.03.045>.
- [12] U. Zerbst, M. Madia, C. Klinger, D. Bettge, Y. Murakami, Defects as a root cause of fatigue failure of metallic components. I: basic aspects, *Eng. Fail. Anal.* 97 (2019) 777–792, <https://doi.org/10.1016/j.engfailanal.2019.01.055>.
- [13] U. Zerbst, M. Madia, C. Klinger, D. Bettge, Y. Murakami, Defects as a root cause of fatigue failure of metallic components. II: non-metallic inclusions, *Eng. Fail. Anal.* (2019) 1–12, <https://doi.org/10.1016/j.engfailanal.2019.01.054>.
- [14] Y. Murakami, C. Klinger, M. Madia, U. Zerbst, D. Bettge, Defects as a root cause of fatigue failure of metallic components. III: cavities, dents, corrosion pits, scratches, *Eng. Fail. Anal.* 97 (2019) 759–776, <https://doi.org/10.1016/j.engfailanal.2019.01.034>.
- [15] A. Du Plessis, S.G. Le Roux, G. Booyen, J. Els, Quality control of a laser additive manufactured medical implant by X-Ray tomography, 3D print, *Addit. Manuf.* 3 (2016) 175–182, <https://doi.org/10.1089/3dp.2016.0012>.
- [16] S. Romano, A. Brandão, J. Gumpinger, M. Gschweilt, S. Beretta, Qualification of AM parts: extreme value statistics applied to tomographic measurements, *Mater. Des.* 131 (2017) 32–48, <https://doi.org/10.1016/j.matdes.2017.05.091>.
- [17] S. Romano, A. Abel, J. Gumpinger, A.D. Brandão, S. Beretta, Quality control of AISI10Mg produced by SLM: metallography versus CT scans for critical defect size assessment, *Addit. Manuf.* 28 (2019) 394–405, <https://doi.org/10.1016/j.addma.2019.05.017>.
- [18] A. du Plessis, S.G. le Roux, Standardized X-ray tomography testing of additively manufactured parts: a round robin test, *Addit. Manuf.* (2018), <https://doi.org/10.1016/J.ADDMA.2018.09.014>.
- [19] I. Yadroitsev, A. Gusarov, I. Yadroitsava, I. Smurov, Single track formation in selective laser melting of metal powders, *J. Mater. Process. Technol.* 210 (2010) 1624–1631, <https://doi.org/10.1016/J.JMATPROTEC.2010.05.010>.
- [20] P. Krakhmalev, I. Yadroitsava, G. Fredriksson, I. Yadroitsev, Microstructural and thermal stability of selective laser melted 316L stainless steel single tracks, *South African J. Ind. Eng.* 28 (2017) 12–19, <https://doi.org/10.7166/28-1-1466>.
- [21] I. Yadroitsev, I. Yadroitsava, P. Bertrand, I. Smurov, Factor analysis of selective laser melting process parameters and geometrical characteristics of synthesized single tracks, *Rapid Prototyp. J.* 18 (2012) 201–208, <https://doi.org/10.1108/13552541211218117>.
- [22] T. Yadroitsev, I. Krakhmalev, P. Yadroitsava, A. Du Plessis, Optimal process parameters for in-situ alloyed Ti15Mo structures by Direct Metal Laser Sintering, *SSF 2017-The 28th Annual International Solid Freeform Fabrication Symposium, Austin, August 7–9, 2017*, pp. 75–96 University of Texas.
- [23] H. Gong, K. Rafi, H. Gu, T. Starr, B. Stucker, Analysis of defect generation in Ti-6Al-4V parts made using powder bed fusion additive manufacturing processes, *Addit. Manuf.* 1 (2014) 87–98, <https://doi.org/10.1016/j.addma.2014.08.002>.
- [24] W.E. King, H.D. Barth, V.M. Castillo, G.F. Gallegos, J.W. Gibbs, D.E. Hahn, C. Kamath, A.M. Rubenchik, Observation of keyhole-mode laser melting in laser powder-bed fusion additive manufacturing, *J. Mater. Process. Technol.* 214 (2014) 2915–2925, <https://doi.org/10.1016/j.jmatprotec.2014.06.005>.
- [25] M. Tang, P.C. Pistorius, J.L. Beuth, Prediction of lack-of-fusion porosity for powder bed fusion, *Addit. Manuf.* 14 (2017) 39–48, <https://doi.org/10.1016/j.addma.2016.12.001>.
- [26] I. Yadroitsev, A. Gusarov, I. Yadroitsava, I. Smurov, Single track formation in selective laser melting of metal powders, *J. Mater. Process. Technol.* 210 (2010) 1624–1631, <https://doi.org/10.1016/J.JMATPROTEC.2010.05.010>.
- [27] S.A. Khairallah, A.T. Anderson, A. Rubenchik, W.E. King, Laser powder-bed fusion additive manufacturing: physics of complex melt flow and formation mechanisms of pores, spatter, and denudation zones, *Acta Mater.* 108 (2016) 36–45, <https://doi.org/10.1016/J.ACTAMAT.2016.02.014>.
- [28] M.J. Matthews, G. Guss, S.A. Khairallah, A.M. Rubenchik, P.J. Depond, W.E. King, Denudation of metal powder layers in laser powder-bed fusion processes, *Addit. Manuf. Handb. Prod. Dev. Def. Ind.* 114 (2017) 677–693, <https://doi.org/10.1201/978131519106>.
- [29] E. Malekipour, H. El-Mounayri, Common defects and contributing parameters in powder bed fusion AM process and their classification for online monitoring and control: a review, *Int. J. Adv. Manuf. Technol.* 95 (2018) 527–550, <https://doi.org/10.1007/s00170-017-1172-6>.
- [30] M. Tang, P.C. Pistorius, J.L. Beuth, Prediction of lack-of-fusion porosity for powder bed fusion, *Addit. Manuf.* 14 (2017) 39–48, <https://doi.org/10.1016/J.ADDMA.2016.12.001>.
- [31] T. Mukherjee, J.S. Zuback, A. De, T. DeRoy, Printability of alloys for additive manufacturing, *Sci. Rep.* 6 (2016) 1–8, <https://doi.org/10.1038/srep19717>.
- [32] M. Bayat, S. Mohanty, J.H. Hattel, Multiphysics modelling of lack-of-fusion voids formation and evolution in IN718 made by multi-track/multi-layer L-PBF, *Int. J. Heat Mass Transf.* 139 (2019) 95–114, <https://doi.org/10.1016/j.ijheatmasstransfer.2019.05.003>.
- [33] C. Zhao, K. Fezzaa, R.W. Cunningham, H. Wen, F. De Carlo, A.D. Rollett, T. Sun, Real-time monitoring of laser powder bed fusion process using high-speed X-ray imaging and diffraction, *Sci. Rep.* 7 (2017) 1–11, <https://doi.org/10.1038/>

- s41598-017-03761-2.
- [34] C.L.A. Leung, S. Marussi, R.C. Atwood, M. Towrie, P.J. Withers, P.D. Lee, In situ X-ray imaging of defect and molten pool dynamics in laser additive manufacturing, *Nat. Commun.* 9 (2018) 1–9, <https://doi.org/10.1038/s41467-018-03734-7>.
- [35] R. Cunningham, C. Zhao, N. Parab, C. Kantzos, J. Pauza, K. Fezzaa, T. Sun, A.D. Rollett, Keyhole threshold and morphology in laser melting revealed by ultrahigh-speed x-ray imaging, *Science* 363 (80-) (2019) 849–852, <https://doi.org/10.1126/science.aav4687>.
- [36] A.A. Martin, N.P. Calta, S.A. Khairallah, J. Wang, P.J. Depond, A.Y. Fong, V. Thampy, G.M. Guss, A.M. Kiss, K.H. Stone, C.J. Tassone, J. Nelson Weker, M.F. Toney, T. van Buuren, M.J. Matthews, Dynamics of pore formation during laser powder bed fusion additive manufacturing, *Nat. Commun.* 10 (2019) 1–10, <https://doi.org/10.1038/s41467-019-10009-2>.
- [37] R. Cunningham, S.P. Narra, C. Montgomery, J. Beuth, A.D. Rollett, Synchrotron-based x-ray microtomography characterization of the effect of processing variables on porosity formation in laser powder-bed additive manufacturing of Ti-6Al-4V, *JOM* 69 (2017) 479–484, <https://doi.org/10.1007/s11837-016-2234-1>.
- [38] R. Cunningham, S.P. Narra, T. Ozturk, J. Beuth, A.D. Rollett, Evaluating the effect of processing parameters on porosity in electron beam melted Ti-6Al-4V via synchrotron X-ray microtomography, *JOM* 68 (2016) 765–771, <https://doi.org/10.1007/s11837-015-1802-0>.
- [39] A. du Plessis, I. Yadroitsev, I. Yadroitsava, S.G. Le Roux, X-ray microcomputed tomography in additive manufacturing: a review of the current technology and applications, *3D print, Addit. Manuf.* 5 (2018), <https://doi.org/10.1089/3dp.2018.0060> 3dp.2018.0060.
- [40] S. Tammas-Williams, H. Zhao, F. Léonard, F. Derguti, I. Todd, P.B. Prangnell, XCT analysis of the influence of melt strategies on defect population in Ti-6Al-4V components manufactured by selective electron beam melting, *Mater. Charact.* 102 (2015) 47–61, <https://doi.org/10.1016/J.MATCHAR.2015.02.008>.
- [41] G. Kasperovich, J. Haubrich, J. Gussone, G. Requena, Correlation between porosity and processing parameters in TiAl6V4 produced by selective laser melting, *Mater. Des.* 105 (2016) 160–170, <https://doi.org/10.1016/J.MATDES.2016.05.070>.
- [43] A. du Plessis, S.G. le Roux, A. Guelpa, The CT Scanner Facility at Stellenbosch University: An open access X-ray computed tomography laboratory, *Nucl. Instruments Methods Phys. Res. Sect. B Beam Interact. Mater. Atoms.* 384 (2016) 42–49, <https://doi.org/10.1016/J.NIMB.2016.08.005>.
- [44] A. du Plessis, P. Sperling, A. Beerlink, L. Tshabalala, S. Hoosain, N. Mathe, G. Stephan, MethodsX Standard method for microCT-based additive manufacturing quality control 1 : porosity analysis, *MethodsX* 5 (2018) 1102–1110, <https://doi.org/10.1016/j.mex.2018.09.005>.